

A Robust Large-Period Discrete Time Crystal and its Signature in a Digital Quantum Computer

Tianqi Chen,^{1,2,3,*} Ruizhe Shen,^{2,†} Ching Hua Lee,^{2,‡} Bo Yang,^{3,4} and Raditya Weda Bomantara^{5,§}

¹*Centre for Quantum Technologies, National University of Singapore, Singapore 117543*

²*Department of Physics, National University of Singapore, Singapore 117542*

³*School of Physical and Mathematical Sciences, Nanyang Technological University, Singapore 639798*

⁴*Institute of High Performance Computing (IHPC),
Agency for Science, Technology and Research (A*STAR),
1 Fusionopolis Way, #16-16 Connexis, Singapore 138632*

⁵*Department of Physics, Interdisciplinary Research Center for Intelligent Secure Systems,
King Fahd University of Petroleum and Minerals, 31261 Dhahran, Saudi Arabia*

Discrete time crystals (DTCs) are novel out-of-equilibrium quantum states of matter which break time translational symmetry. So far, only the simplest form of DTCs that exhibit period-doubling dynamics has been unambiguously realized in experiments. We develop an intuitive interacting spin-1/2 system that supports the more non-trivial period-quadrupling DTCs ($4T$ -DTCs). Remarkably, by utilizing a variational algorithm, we are able to observe clear signatures of such $4T$ -DTCs in a quantum processor despite the presence of considerable noise and the small number of available qubits. Our findings thus demonstrate the feasibility of time crystallinity beyond periodic-doubling, as well as the potential of existing noisy intermediate-scale quantum devices for simulating exotic non-equilibrium quantum states of matter.

INTRODUCTION

The concept of non-ergodicity [1] in quantum phenomena is ubiquitous and important in quantum many-body physics [2]. It underlies a variety of exotic physical phenomena such as eigenstate thermalization hypothesis [3–5], many-body localization [6, 7], quantum scars [8, 9], quantum chaos [10], and time crystals [11–19]. In particular, discrete time crystals (DTCs) [20, 21] are a type of non-ergodic phases of matter that gained prominence in the recent years [22, 23] as the most experimentally realistic form of time crystals. They emerge in periodically driven systems and are characterized by the presence of an order parameter evolving at a period that is robustly locked at an integer multiple of the driving period, persisting indefinitely in the thermodynamic limit [14, 15, 22, 23].

Experimentally realizing DTCs whose order parameter exhibits a much larger period than the corresponding driving period is highly desirable, as it paves the way for observing passive quantum error correction [24], as well as novel dynamical physics such as Anderson localization and Mott insulator transitions in the time domain [25–31]. Therefore, a successful demonstration of period-quadrupling DTCs will further bridge the gap between fundamental studies of DTCs and their technological applications. Unfortunately, despite a considerable number of theoretical proposals for such large-period DTCs [32–38], existing experiments were only able to realize period-doubling [39–44] and period-tripling [45] DTCs. Indeed, as these experiments utilize (pseudo)spin-1/2 particles, they are incompatible with Ref. [32, 33, 35] which utilize bosonic particles. Moreover, with current technology, accessing the very large number of particles with very low to zero noise as required in Refs. [34, 36] is infeasible. Consequently, realizing a large n -tupling DTC in existing systems of spin-1/2 particles is a highly non-trivial task. It is worth noting that a particular example of a period-quadrupling DTC was recently realized in an acoustic system [46]. However, the signature of such a DTC is only observable in the boundaries of the system rather than in its bulk. Moreover, as acoustic systems are inherently classical, the obtained large period DTC may not be directly useful for the aforementioned quantum technological applications.

In this work, we develop an interacting spin-1/2 system that supports period-quadrupling DTCs (which we shall refer to as $4T$ -DTCs) observable even at moderate system sizes. The time-evolution with matrix product states (tMPS) [47, 48] method enables us to numerically investigate, in a controlled manner, the effect of disorder which is necessarily present in the actual quantum devices. Indeed, existing noisy intermediate-scale quantum (NISQ) devices currently possess various kinds of noise, ranging from the relatively poor gate fidelity, the deep circuit depth, to the thermal environment noise rising from the execution of the quantum circuit [49–51]. In this case, the disorder analysis we carry out in the numerical studies simulates the imperfect gate fidelity of NISQ devices. Remarkably, we found that the signatures of $4T$ -DTCs are not only robust against various types of

* tqchen@nus.edu.sg

† ruizhe20@u.nus.edu

‡ phylch@nus.edu.sg

§ raditya.bomantara@kfupm.edu.sa

disorders/gate errors, but can even be amplified in some cases.

Finally, in the efforts towards simulating quantum many-body systems on superconducting quantum processors [52–62], we implement our proposed system in the IBM Q quantum processor *ibmq_cairo*. Despite the various aforementioned noise occurring in our NISQ-era device, a robust period-quadrupling order parameter are clearly observed even at a moderate number of qubits.

RESULTS

4*T*-Discrete Time Crystal

We propose a periodically driven spin-1/2 ladder which is schematically depicted in Fig. 1(a) and described by the following periodically quenched Hamiltonian,

$$\hat{\mathcal{H}}(t) = \begin{cases} \sum_{i=1}^{N_0} -\frac{h}{2} (H_i^{xx} - H_i^{yy}(t)) - JH_i^{zz} & 0 < t < \frac{T}{2}, \\ M \sum_{i=1}^{N_0} \sigma_{i,b}^x & \frac{T}{2} < t < T, \end{cases} \quad (1)$$

where $H_i^{xx} = \sigma_{i,a}^x \sigma_{i,b}^x$, $H_i^{yy}(t) = (1 + \cos \omega t) \sigma_{i,a}^y \sigma_{i,b}^y$, $\tilde{H}_i^{zz} = \sum_{i=1}^{N_0-1} \sigma_{i,a}^z \sigma_{i+1,a}^z$, $\sigma_{i,a/b}^{x/y/z}$ are a set of Pauli matrices describing the spin-1/2 particle at the i -th site of ladder a/b , N_0 is the length of the ladder, $\omega = 2\pi/T$, and T is the driving period. The parameters J and h represent the intra- and inter-ladder interaction strength respectively, whilst M describes the magnetic field strength in a spin-1/2 magnet analogy. Throughout this work, we work in units such that $\hbar = 1$, and set the driving period T to be 1, for easy comparison with the $4T$ time-crystal oscillation period demonstrated later. Note that the Floquet driving appears not just in the 2-step quench, but also in the continuous time dependence of $H_i^{yy}(t)$. In this case, the term $\cos \omega t$ in $H_i^{yy}(t)$ serves to increase the non-integrability of our system, i.e., the evolution operator over one period cannot be written as a mere product of two exponentials.

To understand how Eq. (1) has the propensity to support the sought-after $4T$ -DTC, we first consider the special limit of $hT = MT = \pi$ and $JT = 0$ (to be referred to as the solvable limit hereafter), so that the system reduces to a variation of the model introduced in Ref. [63]. By taking an initial state in which all spins are aligned in the $+z$ -direction, which we denote as $|\uparrow \cdots\rangle_a \otimes |\uparrow \cdots\rangle_b$, it is easily shown (using Eq. (1)) to evolve as [see also Fig. 1(b)]

$$\begin{aligned} |\uparrow \cdots\rangle_a \otimes |\uparrow \cdots\rangle_b &\xrightarrow{(T)} |\downarrow \cdots\rangle_a \otimes |\uparrow \cdots\rangle_b \\ &\xrightarrow{(2T)} |\downarrow \cdots\rangle_a \otimes |\downarrow \cdots\rangle_b \\ &\xrightarrow{(3T)} -|\uparrow \cdots\rangle_a \otimes |\downarrow \cdots\rangle_b \\ &\xrightarrow{(4T)} -|\uparrow \cdots\rangle_a \otimes |\uparrow \cdots\rangle_b. \end{aligned} \quad (2)$$

That is, up to a global phase factor, the state returns to itself only after four periods. Note that if we strictly remain in the non-interacting limit $J = 0$, such $4T$ -periodicity will no longer hold even if the parameters h and M are tuned away from their special parameter values above by the slightest amount. Interestingly, by turning on the inter-site interaction J , our results below show that the above $4T$ -periodicity becomes more robust against such parameters variations. The induced robustness from the interaction of the form $\sigma_{i,a}^z \sigma_{i+1,a}^z$ could be understood from its connection to the physics of the quantum repetition codes [24]. Moreover, As such an interaction renders our system truly many-body in nature, the observed robust $4T$ -periodicity in the vicinity of parameters $hT = MT = \pi$ and $JT = 0$ thus represents a signature of a genuine $4T$ -DTC phase. In the following, we shall demonstrate the stability of this $4T$ -periodic behavior in more detail, for generic parameter values, first through a tMPS numerical simulation, and then alternatively by physically simulating the system on the IBM *ibmq_cairo* quantum processor.

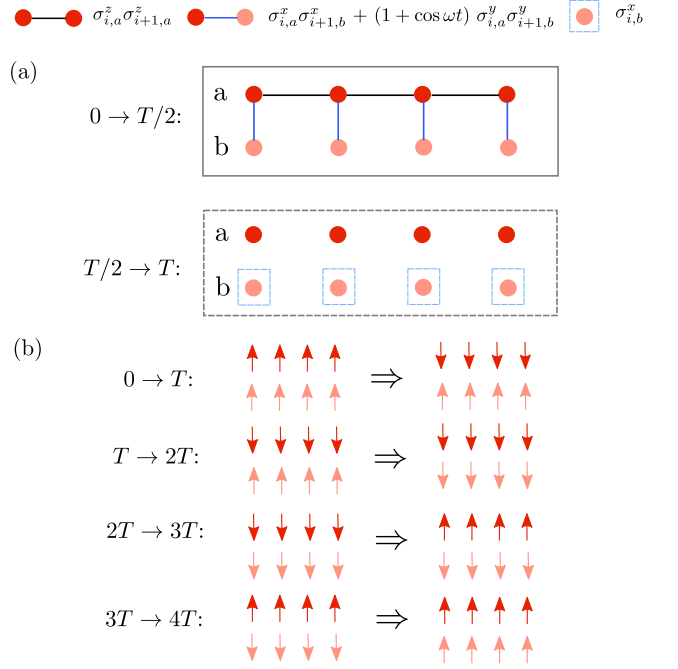


FIG. 1. (a) Schematics of our periodically driven spin-1/2 ladder for $N_0 = 4$. During the first half of the period ($0 \rightarrow T/2$, solid box), the evolution is governed by externally driven Heisenberg spin exchange interactions that are continuously modulated at frequency ω . In the second half of the period ($T/2 \rightarrow T$, dashed box), the interactions are switched off and instead a magnetic field M is applied in the x direction. (b) The $4T$ -periodic oscillations can be intuitively understood in the solvable limit of $JT = 0$ and $hT = MT = \pi$. With all spins initialized pointing up, the system undergoes spatially uniform $4T$ -periodic oscillations; ironically, these oscillations become stabilized if a nonzero JT is introduced. We remark that an additional phase factors of i or (-1) is omitted in the illustration.

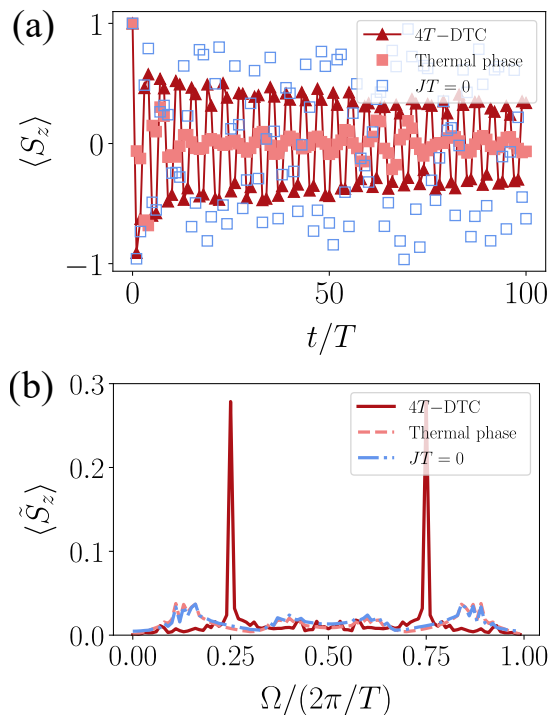


FIG. 2. Numerical evidence of robust 4T-DTC for $N = 16$ sites using tMPS. (a) Magnetization $\langle S_z \rangle$ as a function of time at $MT = 0.98\pi$, which is slightly perturbed away from the “ideal” solvable limit value $MT = \pi$. For $hT = 0.9\pi$, which is also perturbed from π , nonzero interaction strength $JT = 0.16\pi$ (4T-DTC) gives distinctively 4T-periodic oscillations, while $JT = 0$ (blue squares) gives a random-looking pattern. The thermal phase at $JT = 0.1\pi$, $hT = 0.52\pi$ exhibits subdued oscillations. (b) The associated stroboscopic power spectrum $\langle \tilde{S}_z \rangle$, which shows distinct frequency peaks at $\Omega = \pm\pi/2T$ only for the 4T-DTC phase.

Evidence of robust 4T-DTC via tMPS

Here, we employ an efficient method of time evolution with matrix product states (tMPS), where the quantum state is represented as an MPS, and the unitary time evolution operator as a matrix product operator (MPO) [64]. To perform a tMPS study of the system, all the sites are realigned on a linear chain of length $N = 2N_0$ with next-to-nearest neighbor couplings. We then implement a first-order Suzuki-Trotter algorithm with swap gates [65, 66] to carry out the time-evolution, the mathematical details of which could be found in the Methods. The illustration for the tMPS calculation of the model, numerical details, as well as the transformed Hamiltonian, is also shown in the Supplemental Materials.

To capture the signatures of 4T-DTC in our system, we calculate the stroboscopic averaged magnetization dynamics for spins residing on one of the ladders (which we

choose as a)

$$\langle S_z \rangle(t) = \frac{1}{N_0} \sum_{i=1}^{N_0} \langle \sigma_{i,a}^z \rangle(t), \quad (3)$$

and the associated power spectrum as

$$\langle \tilde{S}_z \rangle(\Omega) = \left| \frac{1}{\mathcal{N}_{\text{tot}}} \sum_{k=1}^{\mathcal{N}_{\text{tot}}} \langle S_z \rangle(t) \exp\left\{ \left[-\frac{k\Omega T}{\mathcal{N}_{\text{tot}}} \right] \right\} \right| \quad (4)$$

where \mathcal{N}_{tot} is the total stroboscopic steps evolved, and $t = kT$ ($k = 1, 2, \dots, \mathcal{N}_{\text{tot}}$) is the stroboscopic time at step k . Our results are summarized in Fig. 2 for two different sets of parameter values that correspond to the 4T-DTC phase and the thermal phase respectively. Specifically, as the parameters h and M are chosen close to but not equal to the solvable limit values, at a finite value of the inter-site interaction J , the period-quadrupling feature of $\langle S_z \rangle$ is clearly observed (triangle markers in Fig. 2(a)). This is further demonstrated by a sharp peak at the subharmonic frequency components $\Omega = \pi/2, 3\pi/2$ in the power spectrum of Fig. 2(b). That such a 4T-periodicity is observed over a window of parameter values and not only at a specific set of parameter values suggests that the system indeed supports a 4T-DTC phase. If a parameter h or M deviates significantly from its corresponding ideal value, or if the inter-site interaction J is absent, $\langle S_z \rangle$ quickly decays to zero, and the system is in the thermal phase (empty square and triangle markers in Fig. 2(a)).

In Fig. 3(a), we obtain the phase diagram of the noise-free system by plotting the subharmonic $\Omega T = \pi/2$ peak ($\langle \tilde{S}_z \rangle(\Omega)$ at $\Omega = \pi/2T$) in the power spectrum against the two system parameters h and J . As the value $\Omega = \pi/2T$ represents the fundamental Fourier component of a periodic variable with frequency $\pi/2T$, it is expected that a profile exhibiting a sharp peak at $\Omega = \pi/2T$ is close to being 4T-periodic. We can then associate a finite (zero) $\langle \tilde{S}_z \rangle(\Omega)$ at $\Omega = \pi/2T$ with the 4T-DTC (thermal) phase, of which the amplitude quantifies the 4T-oscillation signature. It is observed that the 4T-DTC phase spans over a considerable window of h values – symmetrically about $hT = \pi$ – at moderate values of J . At $J = 0$, the period-quadrupling feature is observed only at $hT = \pi$, further confirming the role of the inter-site interaction in stabilizing the DTC phase. On the other hand, at very large values of J , the 4T-DTC behavior is absent altogether, which could be attributed to the presence of quantum chaos [67].

In Fig. 3(c,d), we investigate the effect of spatial disorder on our 4T-DTC system, which amounts to replacing the parameters h , J , and M by random values that are respectively drawn from a uniform distribution of $[P - dP + P + dP]$ for each qubit, where $P = h, J, M$ and $dP = dh, dJ, dM$. Specifically, panel (c) [(d)] is chosen so that the mean parameter values are near the border between DTC and thermal phase [deep in the DTC regime].

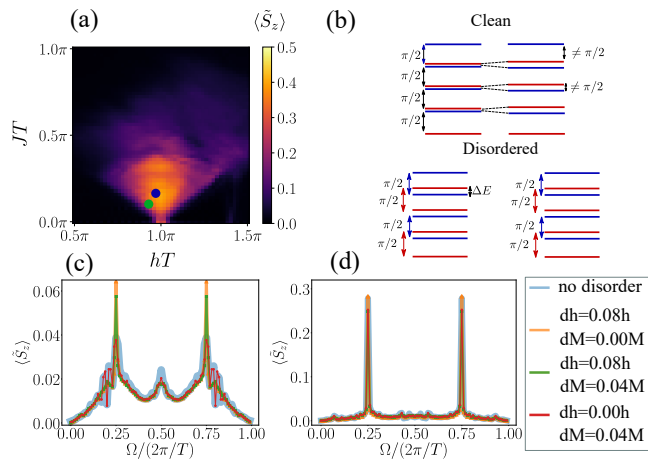


FIG. 3. (a) Presence of $4T$ -DTC behavior over a wide range of JT and hT . The phase diagram representing the value of the subharmonic peak at $\Omega T = \pi/2$ and $MT = 0.98\pi$. (b) Illustration of how partial degeneracy in the clean system (overlapping blue and red lines) leads to the breakdown of the $\pi/2$ quasienergy spacing. The left (right)-side quasienergy spacings correspond to the ones before (after) perturbations. (c-d) The full power spectrum associated with the magnetization dynamics up to $t = 100T$ under the influence of various disorders at (c) $JT = 0.13\pi$, $hT = 0.8\pi$, and $MT = 0.98\pi$, i.e., green dot in panel a, and (d) $JT = 0.16\pi$, $hT = 0.9\pi$, and $MT = 0.98\pi$, i.e., blue dot in panel a. The enhanced subharmonic peaks due to disorders are clearly observed near the DTC-thermal phase boundaries (panel c). All data points involving disorders are averaged over 220 realizations.

Such disorder in turn simulates the effect of gate imperfections in the NISQ device implementation of our $4T$ -DTC. As one disordered parameter might yield a different effect from another, we consider the presence of disorder on one or two parameters at a time in Fig. 3(c,d) for a thorough analysis. Indeed, whilst disorder in the magnetic field M disorder slightly weakens the $\Omega = \pi/2T$ peak (as expected from its role as a noise), the disorder in the interaction parameter h may in fact lead to an enhanced $\Omega = \pi/2T$ peak in some cases (see Fig. 3(c)).

The slight enhancement of the $\Omega = \pi/2T$ peak by some disorder in some cases [see Fig. 3(c)] could be understood as follows. We first recall that in a genuine $4T$ -DTC, a macroscopic number of quasienergies (the eigenphases of the one-period evolution operator) form quadruplets with $\pi/2$ spacing among them, i.e., they can be written as $\varepsilon + n\pi/2$ for some ε and $n = 0, 1, 2, 3$ [24, 63]. Ideally, such quadruplets of quasienergies should be either non-degenerate or fully degenerate ($\varepsilon + n\pi/2$ are degenerate for all n). In the case of partial degeneracy, i.e., $\varepsilon + n\pi/2$ are only degenerate for some n , certain perturbations may nonuniformly shift those degenerate quasienergies [see the upper part of Fig. 3(b)], which then breaks their $\pi/2$ quasienergy spacing and consequently leads to a less robust period-quadrupling signal. In the clean system, such partial degeneracy tends to occur very often; per-

turbing the system parameters near the DTC-thermal phase transitions then causes the many quadruplets of $\pi/2$ -separated quasienergies above to break down due to the aforementioned mechanism. In the presence of spatial disorder, the system parameters for each spin or pair of spins take on slightly different values. As a result, the probability for a system's quasienergy to be degenerate is significantly reduced, thereby resulting in more robust $\pi/2$ -separated quadruplets of quasienergies [see the lower part of Fig. 3(b)]. In the Supplemental Materials, we further demonstrate the above argument by explicitly evaluating the quasienergy levels with and without disorder.

Away from the phase transition boundaries, the presence of disorders does not seem to yield a signal improvement. In some cases, disorders instead slightly reduce the subharmonic peak. Indeed, away from the phase transition boundaries (close to the solvable limit), the detrimental partial degeneracy among different quadruplets of $\pi/2$ -separated quasienergies is already rare to begin with. In this case, disorders instead serve as perturbations in the system parameters with respect to the solvable limit values. Nevertheless, as demonstrated in Fig. 3(c) and (d), our DTC is remarkably robust against moderate disorders ($\sim 8\%$).

Finally, we note that in our numerical results above, we have fixed the system size at $N = 16$ so that it is larger than but remains close to that accessible in our quantum processor implementation below. However, as demonstrated in the Supplemental Materials, qualitatively similar results are also obtained at larger $N = 32$.

Realization of robust $4T$ -DTC on a quantum processor

Being a NISQ device, the currently available quantum processors inevitably exhibit various types of device noise. Among these, quantum gate imperfections, which simulate the time-evolution of some disordered Hamiltonian, are the most significant sources of noise for simulating short- to moderate-time dynamics [57]. That our tMPS numerical simulations of the model above have demonstrated the extremely robust signatures of $4T$ -DTC in the presence of such a noise in turn suggests the feasibility for implementation on a quantum computer.

Here, we proceed to realize our system and capture its DTC signatures on the IBMQ quantum processor. Naive implementation of the time dynamics of our model in a quantum circuit follows from a similar trotterization procedure as in our tMPS simulations, and more details are shown in the Supplemental Materials. For any quantum circuit implementation, the coupling between qubits needs to be implemented via basic quantum gates such as the controlled NOT (CNOT) and the single-qubit rotation gates; one significant advantage of a quantum circuit implementation over other quantum platforms, e.g., ultracold atoms, is that a time-dependent model such as our DTC model can be implemented without any addi-

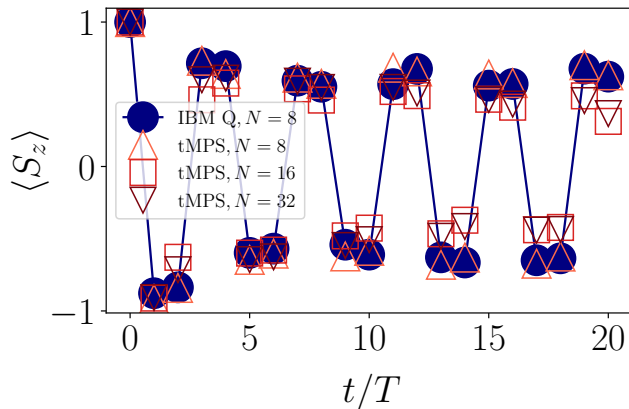


FIG. 4. Physical signature of $4T$ -DTC behavior on the IBM quantum processor and its comparison with tMPS results at several system sizes (green). The parameters used are: $JT = 0.16\pi$, $MT = 0.98\pi$, $hT = 0.9\pi$. For the details of the device *ibmq_cairo* and its error information, see Fig. S5 in the Supplemental Materials.

tional difficulty, just by concatenating different Trotter steps at different stages. Instead of transpiling local couplings within each Trotter step, we adopt a more efficient approach by leveraging the variational circuit optimization technique, and the details of this approach are presented in the Supplemental Materials. This strategy of directly implementing the whole circuit requires fewer CX gates and compresses the circuit depth, thereby suppressing the effect of gate error. For other simulations using the Trotterization approach [68, 69], the signature of the DTC gets poorer after every Floquet cycle under the evolving dynamics, as the circuit depth itself grows linearly. In our unique scheme of trained circuits with a fixed circuit depth, as demonstrated below, we successfully achieve robust results for our proposed $4T$ -DTC model, and in particular, it exhibits remarkably strong resilience to device noise even after many Floquet cycles. In the Supplemental Materials, we have also numerically simulated the system by using the direct Trotterization approach and found that a slightly smaller noise level than that in the actual NISQ device is required to observe a clear $4T$ -DTC signature. This in turn shows that our variational circuit optimization approach remains to be the more feasible approach to implement large-period DTCs on a present quantum computer.

In Fig. 4, we present the stroboscopic magnetization $\langle S_z \rangle$ (solid circles) obtained from the IBM quantum computer over time dynamics and compare these with the numerical results (unfilled circles, squares, and triangles) obtained by the tMPS method. Remarkably, thanks to our variational method, the quantum simulation over long periods of time (20 Floquet steps) is possible. Within such long-time dynamics, our numerical and quantum results demonstrate an excellent agreement, indicating that our IBM Q simulation gives a perfect char-

acterization of our $4T$ -DTC model. Here, we execute our IBM Q simulation on an 8-qubit case which enables the realization of highly-compressed trained circuits for overcoming device noise¹. This is already a sufficiently long chain for demonstrating $4T$ -DTC since we find that finite-size effects are qualitatively insignificant, i.e., our tMPS results at different sizes all show qualitatively similar profiles with the IBM Q results, both deep in the DTC regime and near the boundaries with the thermal phase (see Fig. 4 and S4 in the Supplemental Materials).

DISCUSSION

We proposed an intuitive and realistic spin-1/2 model that supports a nontrivial type of DTC, characterized by a robust period-quadrupling observable rather than the more common period-doubling type. Remarkably, we were able to explicitly capture the signatures of such $4T$ -DTC both numerically and via a NISQ-era IBM quantum processor, even at relatively small number of qubits and in the presence of considerable hardware noise (some disorder actually yields slight enhancements in the $4T$ -DTC signatures in some cases). Remarkably, the two approaches yield excellent agreement even though the noise in the quantum processor cannot be exactly replicated in the numerical simulation.

The experimental realization of our $4T$ -DTC system at larger system sizes is expected to be a significant future research direction, both in the area of quantum computing and in condensed matter platforms such as ultracold atoms [43, 70–79]. On the one hand, that our $4T$ -DTC phase exists within a spin-1/2 system makes it a realistic and appropriate phenomenon for benchmarking the performance of various existing noisy intermediate-scale quantum (NISQ) devices. On the other hand, the ability to achieve a large size $4T$ -DTC may also open up opportunities to harness its technological application beyond observing its subharmonic signatures, e.g., as a quantum memory or a passive quantum error correcting device. Finally, a realistic generalization of our spin-1/2 system construction that supports DTCs beyond period-quadrupling makes for a good avenue for future theoretical and experimental studies that can uncover rich phenomenology lying in the intersection of Floquet, many-body or even non-Hermitian physics.

¹ Our IBM Q simulation is scalable. Detailed discussion is shown in the Supplemental Materials.

METHODS

Details of Suzuki-Trotter decomposition and time evolution on IBM Q

We start by discussing how to simulate the dynamics of our model in Eq. (6) on a quantum circuit digitally. First, within each period T , the time evolution operator \hat{U} operates as

$$\hat{U}|\psi_0\rangle = \hat{U}_{T/2 \rightarrow T} \hat{U}_{0 \rightarrow T/2} |\psi_0\rangle \quad (5)$$

where $|\psi_0\rangle$ is the initial state, $\hat{U}_{0 \rightarrow T/2}$ is the evolution operator for the first-half period, and $\hat{U}_{T/2 \rightarrow T}$ is the evolution operator for the second-half period. We remark that for the tMPS simulation, the total system needs to

$$\hat{U}_{0 \rightarrow T/2} \approx \prod_{n=0}^{T/\delta t} \left[\prod_{i=0}^{N/4-1} e^{+i\delta t J \sigma_{2i+2}^z \otimes I_{2i+3} \otimes \sigma_{2i+4}^z} \prod_{i=0}^{N/4} e^{+i\delta t J \sigma_{2i}^z \otimes I_{2i+1} \otimes \sigma_{2i+2}^z} \right] \left[\prod_{i=0}^{N/2} e^{+i\delta t h/2 (\sigma_{2i}^x \otimes \sigma_{2i+1}^x - (1 + \cos \omega n \delta t) \sigma_{2i}^y \otimes \sigma_{2i+1}^y)} \right], \quad (8)$$

where δt is the discretized time step, which is set to be $0.01/T$ ($T = 1$) in our numerics. Note that for the next-nearest neighbor coupling terms in the above expression, for the simulation on IBM Q, it only requires a pair of swap gates between the ancilla qubit ($i = 4$) and the physical qubit ($i = 6$) with system size $N = 8$ [see Fig. S5(d) in the Supplementary Materials], while for the simulation with tMPS, since it is aligned to a linear spin chain, for a system size of N (assume N is always even in this case), it requires $(N/2 - 1)$ pairs of the swap gates [65, 66]. Finally, the second-half time evolution operator $\hat{U}_{T/2 \rightarrow T}$ can be simply realized by the following R_x rotations

$$\hat{U}_{T/2 \rightarrow T} = \prod_{i=0}^{N/2} e^{-i \frac{MT}{2} \sigma_{2i+1}^x}. \quad (9)$$

Throughout this manuscript, we take the evolution time step for our tMPS algorithm as $0.01\hbar$, and the convergences of the tMPS calculations are confirmed by checking the truncation errors after repeating the runs for different values of the maximum bond dimension. We find that keeping a maximum auxiliary bond dimension of 100 (60) for $N = 24, 32$ ($N = 8, 16$) for all tMPS calculations allows us to produce precise simulations, with errors on the observables of, at most, 10^{-8} .

be aligned as a linear chain with some of the terms having next-nearest neighbor couplings [see Fig. 5], and the Hamiltonian thus becomes

$$\hat{\mathcal{H}}(t) = \begin{cases} -\hbar/2 \sum_{i=1}^{N_0} (H_i^{xx} - H_i^{yy}) - JH_i^{zz} & 0 < t < \frac{T}{2}, \\ M \sum_{i=1}^{N_0} \sigma_{2i}^x & \frac{T}{2} < t < T. \end{cases} \quad (6)$$

where

$$\begin{aligned} H_i^{xx} &= \sigma_{2i-1}^x \sigma_{2i}^x \\ H_i^{yy} &= (1 + \cos \omega t) \sigma_{2i-1}^y \sigma_{2i}^y \\ H_i^{zz} &= \sum_{i=1}^{N_0-1} \sigma_{2i-1}^z \sigma_{2i+1}^z \end{aligned} \quad (7)$$

For each half period, we could therefore consider applying the first-order Suzuki-Trotter decomposition, and obtain the first half of U as follows

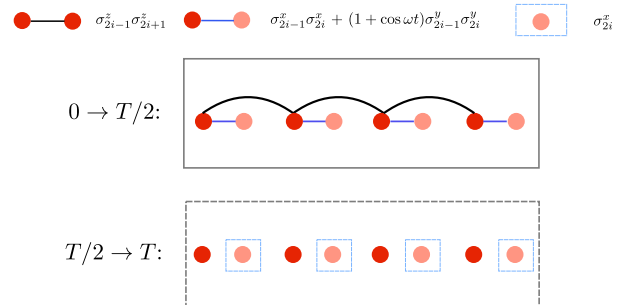


FIG. 5. Illustration of schematical tMPS with Suzuki-Trotter decomposition. The total system from Fig. 1 of the main text is now mapped into a single chain with alternative nearest neighbor and next-nearest neighbor couplings.

Variational quantum algorithm for the time evolution on IBM Q

Here, we provide the essential details of our variational quantum circuit recompilation for the time evolution operators used in the main text. The scheme of our variational algorithm to obtain the parametrized quantum circuit is depicted in Fig. S5(c) and (d) in the Supplementary Materials. The original time evolution circuit \hat{U} with Suzuki-Trotter gates is transformed into a Trot-

terized ansatz circuit $\hat{\mathcal{V}}$ via variational optimization [see Fig. S5(c) in the Supplementary Materials]. For each stroboscopic time step $t = kT$ ($k = 1, 2, \dots, \mathcal{N}_{\text{tot}}$), it is transformed into an ansatz $\hat{\mathcal{V}}(t = kT)$, which consists of an initial layer of U_3 gates followed by concatenated odd layers (green) and even layers (purple)[Fig. S5(c) in the Supplementary Materials], which has a Trotterized time evolution pattern. Here, we set all number of total layers to be equal to be three, i.e. it has in total three combined layers of odd and even layers.

The circuit variational optimization is done by minimizing the cost function

$$F(\hat{\mathcal{U}}, \hat{\mathcal{V}}) = 1 - \langle \psi_0 | \hat{\mathcal{V}}^\dagger \hat{\mathcal{U}} | \psi_0 \rangle \quad (10)$$

where we have deliberately chosen the initial $|\psi_0\rangle$ with all sites in $|\uparrow\rangle$. The process of the circuit variational optimization involves optimizing a $3D$ rotation gate labeled as $U_3(\theta, \phi, \lambda)$. This gate is characterized by three rotational parameters which are variable: θ , ϕ and λ . We refer to the Supplementary Materials for other details of the optimization.

Measurement of observables on IBM Q

The magnetization in the z direction for each spin residing on ladder a from our model is obtained via the measurement procedure on IBM quantum processor, which is performed after the time evolution in the Trotterized ansatz circuit $\hat{\mathcal{V}}$. On IBM Q, the measured outcomes are all represented in binary bit strings, i.e. 0 for spin-up ($|\uparrow\rangle$), and 1 for spin-down ($|\downarrow\rangle$). For each site i , the magnetization in the z direction for each spin residing on ladder a $\langle \sigma_{i,a}^z \rangle$ is computed as

$$\langle \sigma_{i,a}^z \rangle = \langle \sigma_{i,a}^\uparrow \rangle - \langle \sigma_{i,a}^\downarrow \rangle \quad (11)$$

$$\text{where } \sigma^\uparrow = \begin{pmatrix} 1 & 0 \\ 0 & 0 \end{pmatrix}, \text{ and } \sigma^\downarrow = \begin{pmatrix} 0 & 0 \\ 0 & 1 \end{pmatrix}.$$

Then, the stroboscopic averaged magnetization dynamics from Eq. 3 as well as the associated power spectrum from Eq. 4 can all be easily obtained from the above results.

DATA AVAILABILITY

The data that supports the findings of this study are available from the corresponding author upon request.

CODE AVAILABILITY

The code used for this paper is available upon reasonable requests from the corresponding authors.

AUTHOR CONTRIBUTIONS

R. W. .B. proposed the initial idea, and developed the $4T$ -DTC model. C. H. L. and R. W. .B. guided the overall research direction and supervised this work. T. C. performed the classical simulations using tMPS, and also developed the algorithms and implemented them on the IBM Q. R. S. developed part of the algorithms on IBM Q and proposed the idea of the circuit recompilation. Y. B. contributed to part of the discussions. All the authors contributed to the writing of the manuscript.

ACKNOWLEDGMENTS

We are grateful to Jiangbin Gong for fruitful discussions. T. C. thanks E. Miles Stoudenmire for fruitful discussion via ITensor discourse group (<https://itensor.discourse.group/>). T. C. and R. S. thank Truman Ng and Russell Yang for discussions on the quantum simulation implementation on IBM Quantum services. C. H. L. and T. C. acknowledges support by Singapore's NRF Quantum engineering grant NRF2021-QEP2-02-P09 and Singapore's MOE Tier-II grant (MOE-T2EP50222-0003). T. C. and B. Y. acknowledges the support from Singapore National Research Foundation (NRF) under NRF fellowship award NRF-NRFF12-2020-0005. R. W. B acknowledges the support provided by the Deanship of Research Oversight and Coordination (DROC) at King Fahd University of Petroleum & Minerals (KFUPM) through project No. EC221010. We acknowledge the use of IBM Quantum services for this work. The views expressed are those of the authors, and do not reflect the official policy or position of IBM or the IBM Quantum team. The MPS calculation in this work is performed using ITensor library [80]. The computational work for this article was partially performed on resources of the National Supercomputing Centre, Singapore (<https://www.nsc.sg/>), and on the National University of Singapore (NUS)'s high-performance computing facilities.

[1] R. J. Hardy and C. Binek, *Thermodynamics and statistical mechanics: an integrated approach* (John Wiley & Sons, 2014).

[2] P. W. Anderson, More is different, *Science* **177**, 393 (1972).

[3] J. M. Deutsch, Quantum statistical mechanics in a closed system, *Phys. Rev. A* **43**, 2046 (1991).

- [4] M. Srednicki, Chaos and quantum thermalization, *Phys. Rev. E* **50**, 888 (1994).
- [5] C. Murthy, A. Babakhani, F. Iniguez, M. Srednicki, and N. Yunger Halpern, Non-abelian eigenstate thermalization hypothesis, *Phys. Rev. Lett.* **130**, 140402 (2023).
- [6] R. Nandkishore and D. A. Huse, Many-body localization and thermalization in quantum statistical mechanics, *Annu. Rev. Condens. Matter Phys.* **6**, 15 (2015).
- [7] D. A. Abanin, E. Altman, I. Bloch, and M. Serbyn, Colloquium: Many-body localization, thermalization, and entanglement, *Rev. Mod. Phys.* **91**, 021001 (2019).
- [8] M. Serbyn, D. A. Abanin, and Z. Papić, Quantum many-body scars and weak breaking of ergodicity, *Nature Physics* **17**, 675 (2021).
- [9] A. Chandran, T. Iadecola, V. Khemani, and R. Moessner, Quantum many-body scars: A quasiparticle perspective, *Annual Review of Condensed Matter Physics* **14**, 443 (2023).
- [10] L. D'Alessio, Y. Kafri, A. Polkovnikov, and M. Rigol, From quantum chaos and eigenstate thermalization to statistical mechanics and thermodynamics, *Advances in Physics* **65**, 239 (2016).
- [11] F. Wilczek, Quantum time crystals, *Phys. Rev. Lett.* **109**, 160401 (2012).
- [12] P. Bruno, Impossibility of spontaneously rotating time crystals: A no-go theorem, *Phys. Rev. Lett.* **111**, 070402 (2013).
- [13] H. Watanabe and M. Oshikawa, Absence of quantum time crystals, *Phys. Rev. Lett.* **114**, 251603 (2015).
- [14] K. Sacha and J. Zakrzewski, Time crystals: a review, *Reports on Progress in Physics* **81**, 016401 (2017).
- [15] V. Khemani, R. Moessner, and S. Sondhi, A brief history of time crystals, [arXiv:1910.10745](https://arxiv.org/abs/1910.10745) (2019).
- [16] S. Autti, V. B. Eltsov, and G. E. Volovik, Observation of a time quasicrystal and its transition to a superfluid time crystal, *Phys. Rev. Lett.* **120**, 215301 (2018).
- [17] B. Huang, Y.-H. Wu, and W. V. Liu, Clean floquet time crystals: Models and realizations in cold atoms, *Phys. Rev. Lett.* **120**, 110603 (2018).
- [18] S. Autti, P. J. Heikkinen, J. Nissinen, J. T. Mäkinen, G. E. Volovik, V. Zavyalov, and V. B. Eltsov, Nonlinear two-level dynamics of quantum time crystals, *Nature communications* **13**, 3090 (2022).
- [19] B. Huang, T.-H. Leung, D. M. Stamper-Kurn, and W. V. Liu, Discrete time crystals enforced by floquet-bloch scars, *Phys. Rev. Lett.* **129**, 133001 (2022).
- [20] N. Y. Yao, A. C. Potter, I.-D. Potirniche, and A. Vishwanath, Discrete time crystals: Rigidity, criticality, and realizations, *Phys. Rev. Lett.* **118**, 030401 (2017).
- [21] D. V. Else, B. Bauer, and C. Nayak, Floquet time crystals, *Phys. Rev. Lett.* **117**, 090402 (2016).
- [22] D. V. Else, C. Monroe, C. Nayak, and N. Y. Yao, Discrete time crystals, *Annual Review of Condensed Matter Physics* **11**, 467 (2020).
- [23] M. P. Zaletel, M. Lukin, C. Monroe, C. Nayak, F. Wilczek, and N. Y. Yao, Colloquium: Quantum and classical discrete time crystals, *Rev. Mod. Phys.* **95**, 031001 (2023).
- [24] R. W. Bomantara, Quantum repetition codes as building blocks of large-period discrete time crystals, *Phys. Rev. B* **104**, L180304 (2021).
- [25] L. Guo, M. Marthaler, and G. Schön, Phase space crystals: A new way to create a quasienergy band structure, *Phys. Rev. Lett.* **111**, 205303 (2013).
- [26] K. Sacha, Anderson localization and mott insulator phase in the time domain, *Scientific reports* **5**, 10787 (2015).
- [27] D. Delande, L. Morales-Molina, and K. Sacha, Three-dimensional localized-delocalized anderson transition in the time domain, *Phys. Rev. Lett.* **119**, 230404 (2017).
- [28] K. Giergiel and K. Sacha, Anderson localization of a rydberg electron along a classical orbit, *Phys. Rev. A* **95**, 063402 (2017).
- [29] M. Mierzejewski, K. Giergiel, and K. Sacha, Many-body localization caused by temporal disorder, *Phys. Rev. B* **96**, 140201 (2017).
- [30] K. Giergiel, A. Miroszewski, and K. Sacha, Time crystal platform: From quasicrystal structures in time to systems with exotic interactions, *Phys. Rev. Lett.* **120**, 140401 (2018).
- [31] L. Guo and P. Liang, Condensed matter physics in time crystals, *New Journal of Physics* **22**, 075003 (2020).
- [32] K. Sacha, Modeling spontaneous breaking of time-translation symmetry, *Phys. Rev. A* **91**, 033617 (2015).
- [33] F. M. Surace, A. Russomanno, M. Dalmonte, A. Silva, R. Fazio, and F. Iemini, Floquet time crystals in clock models, *Phys. Rev. B* **99**, 104303 (2019).
- [34] P. Nurwanto, R. W. Bomantara, and J. Gong, Discrete time crystals in many-body quantum chaos, *Phys. Rev. B* **100**, 214311 (2019).
- [35] K. Giergiel, T. Tran, A. Zaheer, A. Singh, A. Sidorov, K. Sacha, and P. Hannaford, Creating big time crystals with ultracold atoms, *New Journal of Physics* **22**, 085004 (2020).
- [36] A. Pizzi, J. Knolle, and A. Nunnenkamp, Higher-order and fractional discrete time crystals in clean long-range interacting systems, *Nature communications* **12**, 2341 (2021).
- [37] A. Kshetrimayum, M. Goihl, D. M. Kennes, and J. Eisert, Quantum time crystals with programmable disorder in higher dimensions, *Phys. Rev. B* **103**, 224205 (2021).
- [38] M. H. Muñoz Arias, K. Chinni, and P. M. Poggi, Floquet time crystals in driven spin systems with all-to-all p -body interactions, *Phys. Rev. Res.* **4**, 023018 (2022).
- [39] J. Zhang, P. W. Hess, A. Kyprianidis, P. Becker, A. Lee, J. Smith, G. Pagano, I.-D. Potirniche, A. C. Potter, A. Vishwanath, *et al.*, Observation of a discrete time crystal, *Nature* **543**, 217 (2017).
- [40] J. Rovny, R. L. Blum, and S. E. Barrett, Observation of discrete-time-crystal signatures in an ordered dipolar many-body system, *Phys. Rev. Lett.* **120**, 180603 (2018).
- [41] J. Rovny, R. L. Blum, and S. E. Barrett, ^{31}P nmr study of discrete time-crystalline signatures in an ordered crystal of ammonium dihydrogen phosphate, *Phys. Rev. B* **97**, 184301 (2018).
- [42] S. Pal, N. Nishad, T. S. Mahesh, and G. J. Sreejith, Temporal order in periodically driven spins in star-shaped clusters, *Phys. Rev. Lett.* **120**, 180602 (2018).
- [43] A. Kyprianidis, F. Machado, W. Morong, P. Becker, K. S. Collins, D. V. Else, L. Feng, P. W. Hess, C. Nayak, G. Pagano, *et al.*, Observation of a prethermal discrete time crystal, *Science* **372**, 1192 (2021).
- [44] K. Shinjo, K. Seki, T. Shirakawa, R.-Y. Sun, and S. Yunoki, Unveiling clean two-dimensional discrete time quasicrystals on a digital quantum computer, [arXiv:2403.16718](https://arxiv.org/abs/2403.16718) (2024).

- [45] S. Choi, J. Choi, R. Landig, G. Kucsko, H. Zhou, J. Isoya, F. Jelezko, S. Onoda, H. Sumiya, V. Khemani, *et al.*, Observation of discrete time-crystalline order in a disordered dipolar many-body system, *Nature* **543**, 221 (2017).
- [46] Z. Cheng, R. W. Bomantara, H. Xue, W. Zhu, J. Gong, and B. Zhang, Observation of $\pi/2$ modes in an acoustic floquet system, *Phys. Rev. Lett.* **129**, 254301 (2022).
- [47] G. Vidal, Efficient simulation of one-dimensional quantum many-body systems, *Phys. Rev. Lett.* **93**, 040502 (2004).
- [48] S. Paeckel, T. Köhler, A. Swoboda, S. R. Manmana, U. Schollwöck, and C. Hubig, Time-evolution methods for matrix-product states, *Annals of Physics* **411**, 167998 (2019).
- [49] J. Preskill, Quantum Computing in the NISQ era and beyond, *Quantum* **2**, 79 (2018).
- [50] S. Johnston and J.-F. Van Huele, Understanding and compensating for noise on ibm quantum computers, *American Journal of Physics* **89**, 935 (2021).
- [51] J. W. Z. Lau, K. H. Lim, H. Shrotriyi, and L. C. Kwek, Nisq computing: where are we and where do we go?, *AAPPS Bulletin* **32**, 27 (2022).
- [52] A. Smith, M. Kim, F. Pollmann, and J. Knolle, Simulating quantum many-body dynamics on a current digital quantum computer, *npj Quantum Information* **5**, 106 (2019).
- [53] A. Rahmani, K. J. Sung, H. Putterman, P. Roushan, P. Ghaemi, and Z. Jiang, Creating and manipulating a Laughlin-type $\nu = 1/3$ fractional quantum hall state on a quantum computer with linear depth circuits, *PRX Quantum* **1**, 020309 (2020).
- [54] Google AI Quantum and Collaborators, F. Arute, K. Arya, R. Babbush, D. Bacon, J. C. Bardin, R. Barends, S. Boixo, M. Broughton, B. B. Buckley, *et al.*, Hartree-fock on a superconducting qubit quantum computer, *Science* **369**, 1084 (2020).
- [55] A. Kirmani, K. Bull, C.-Y. Hou, V. Saravanan, S. M. Saeed, Z. Papić, A. Rahmani, and P. Ghaemi, Probing geometric excitations of fractional quantum hall states on quantum computers, *Phys. Rev. Lett.* **129**, 056801 (2022).
- [56] X. Mi, M. Ippoliti, C. Quintana, A. Greene, Z. Chen, J. Gross, F. Arute, K. Arya, J. Atalaya, R. Babbush, *et al.*, Time-crystalline eigenstate order on a quantum processor, *Nature* **601**, 531 (2022).
- [57] P. Frey and S. Rachel, Realization of a discrete time crystal on 57 qubits of a quantum computer, *Science Advances* **8**, 7652 (2022).
- [58] J. M. Koh, T. Tai, and C. H. Lee, Simulation of interaction-induced chiral topological dynamics on a digital quantum computer, *Phys. Rev. Lett.* **129**, 140502 (2022).
- [59] T. Chen, R. Shen, C. H. Lee, and B. Yang, High-fidelity realization of the AKLT state on a NISQ-era quantum processor, *SciPost Phys.* **15**, 170 (2023).
- [60] J. M. Koh, T. Tai, and C. H. Lee, Observation of higher-order topological states on a quantum computer, [arXiv:2303.02179](https://arxiv.org/abs/2303.02179) (2023).
- [61] Y. Kim, A. Eddins, S. Anand, K. X. Wei, E. Van Den Berg, S. Rosenblatt, H. Nayfeh, Y. Wu, M. Zaletel, K. Temme, *et al.*, Evidence for the utility of quantum computing before fault tolerance, *Nature* **618**, 500 (2023).
- [62] Z.-C. Xiang, K. Huang, Y.-R. Zhang, T. Liu, Y.-H. Shi, C.-L. Deng, T. Liu, H. Li, G.-H. Liang, Z.-Y. Mei, *et al.*, Simulating chern insulators on a superconducting quantum processor, *Nature Communications* **14**, 5433 (2023).
- [63] R. W. Bomantara, Square-root floquet topological phases and time crystals, *Phys. Rev. B* **106**, L060305 (2022).
- [64] B. Pirvu, V. Murg, J. I. Cirac, and F. Verstraete, Matrix product operator representations, *New Journal of Physics* **12**, 025012 (2010).
- [65] M. Suzuki, Fractal decomposition of exponential operators with applications to many-body theories and monte carlo simulations, *Physics Letters A* **146**, 319 (1990).
- [66] E. M. Stoudenmire and S. R. White, Minimally entangled typical thermal state algorithms, *New Journal of Physics* **12**, 055026 (2010).
- [67] A. Russomanno, F. Iemini, M. Dalmonte, and R. Fazio, Floquet time crystal in the Lipkin-Meshkov-Glick model, *Phys. Rev. B* **95**, 214307 (2017).
- [68] H. Xu, J. Zhang, J. Han, Z. Li, G. Xue, W. Liu, Y. Jin, and H. Yu, Realizing discrete time crystal in an one-dimensional superconducting qubit chain (2021).
- [69] C. Sims, Simulation of higher-dimensional discrete time crystals on a quantum computer, *Crystals* **13** (2023).
- [70] M. Greiner, O. Mandel, T. Esslinger, T. W. Hänsch, and I. Bloch, Quantum phase transition from a superfluid to a mott insulator in a gas of ultracold atoms, *Nature* **415**, 39 (2002).
- [71] I. Bloch, Ultracold quantum gases in optical lattices, *Nature Physics* **1**, 23 (2005).
- [72] I. Bloch, J. Dalibard, and W. Zwerger, Many-body physics with ultracold gases, *Rev. Mod. Phys.* **80**, 885 (2008).
- [73] I. Bloch, J. Dalibard, and S. Nascimbene, Quantum simulations with ultracold quantum gases, *Nature Physics* **8**, 267 (2012).
- [74] H. Miyake, G. A. Siviloglou, C. J. Kennedy, W. C. Burton, and W. Ketterle, Realizing the Harper Hamiltonian with laser-assisted tunneling in optical lattices, *Phys. Rev. Lett.* **111**, 185302 (2013).
- [75] G. Jotzu, M. Messer, R. Desbuquois, M. Lebrat, T. Uehlinger, D. Greif, and T. Esslinger, Experimental realization of the topological Haldane model with ultracold fermions, *Nature* **515**, 237 (2014).
- [76] M. Schreiber, S. S. Hodgman, P. Bordia, H. P. Lüschen, M. H. Fischer, R. Vosk, E. Altman, U. Schneider, and I. Bloch, Observation of many-body localization of interacting fermions in a quasirandom optical lattice, *Science* **349**, 842 (2015).
- [77] A. Mazurenko, C. S. Chiu, G. Ji, M. F. Parsons, M. Kanász-Nagy, R. Schmidt, F. Grusdt, E. Demler, D. Greif, and M. Greiner, A cold-atom fermi-hubbard antiferromagnet, *Nature* **545**, 462 (2017).
- [78] G. Salomon, J. Koepsell, J. Vijayan, T. A. Hilker, J. Nešpolo, L. Pollet, I. Bloch, and C. Gross, Direct observation of incommensurate magnetism in Hubbard chains, *Nature* **565**, 56 (2019).
- [79] R. Shen, T. Chen, M. M. Aliyu, F. Qin, Y. Zhong, H. Loh, and C. H. Lee, Proposal for observing Yang-Lee criticality in Rydberg atomic arrays, *Phys. Rev. Lett.* **131**, 080403 (2023).
- [80] M. Fishman, S. R. White, and E. M. Stoudenmire, The ITensor Software Library for Tensor Network Calcula-

- tions, *SciPost Phys. Codebases* , 4 (2022).
- [81] M. Cerezo, A. Arrasmith, R. Babbush, S. C. Benjamin, S. Endo, K. Fujii, J. R. McClean, K. Mitarai, X. Yuan, L. Cincio, *et al.*, Variational quantum algorithms, *Nature Reviews Physics* **3**, 625 (2021).
- [82] L. Bittel and M. Kliesch, Training variational quantum algorithms is np-hard, *Phys. Rev. Lett.* **127**, 120502 (2021).
- [83] K. Heya, Y. Suzuki, Y. Nakamura, and K. Fujii, Variational quantum gate optimization, [arXiv:1810.12745](https://arxiv.org/abs/1810.12745) (2018).
- [84] S. Khatiri, R. LaRose, A. Poremba, L. Cincio, A. T. Sornborger, and P. J. Coles, Quantum-assisted quantum compiling, *Quantum* **3**, 140 (2019).
- [85] S.-N. Sun, M. Motta, R. N. Tazhigulov, A. T. Tan, G. K.-L. Chan, and A. J. Minnich, Quantum computation of finite-temperature static and dynamical properties of spin systems using quantum imaginary time evolution, *PRX Quantum* **2**, 010317 (2021).
- [86] J. M. Koh, T. Tai, Y. H. Phee, W. E. Ng, and C. H. Lee, Stabilizing multiple topological fermions on a quantum computer, *npj Quantum Information* **8**, 16 (2022).
- [87] J. M. Koh, T. Tai, and C. H. Lee, Simulation of interaction-induced chiral topological dynamics on a digital quantum computer, *Phys. Rev. Lett.* **129**, 140502 (2022).
- [88] J. Gray, quimb: a python library for quantum information and many-body calculations, *Journal of Open Source Software* **3**, 819 (2018).
- [89] A. T. K. Tan, S.-N. Sun, R. N. Tazhigulov, G. K.-L. Chan, and A. J. Minnich, Realizing symmetry-protected topological phases in a spin-1/2 chain with next-nearest-neighbor hopping on superconducting qubits, *Phys. Rev. A* **107**, 032614 (2023).
- [90] Qiskit contributors, *Qiskit: An open-source framework for quantum computing* (2023).
- [91] R. Malouf, A comparison of algorithms for maximum entropy parameter estimation, in *Proceedings of the 6th Conference on Natural Language Learning - Volume 20*, COLING-02 (Association for Computational Linguistics, USA, 2002) p. 1–7.
- [92] G. Andrew and J. Gao, Scalable training of l1-regularized log-linear models, in *Proceedings of the 24th International Conference on Machine Learning*, ICML '07 (Association for Computing Machinery, New York, NY, USA, 2007) p. 33–40.
- [93] Z. Li and H. A. Scheraga, Monte carlo-minimization approach to the multiple-minima problem in protein folding., *Proceedings of the National Academy of Sciences* **84**, 6611 (1987).
- [94] D. J. Wales and J. P. K. Doye, Global Optimization by Basin-Hopping and the Lowest Energy Structures of Lennard-Jones Clusters Containing up to 110 Atoms, *The Journal of Physical Chemistry A* **101**, 5111 (1997).
- [95] D. J. Wales and H. A. Scheraga, Global optimization of clusters, crystals, and biomolecules, *Science* **285**, 1368 (1999).
- [96] D. Wales, *Energy Landscapes: Applications to Clusters, Biomolecules and Glasses*, Cambridge Molecular Science (Cambridge University Press, 2004).
- [97] K. Temme, S. Bravyi, and J. M. Gambetta, Error mitigation for short-depth quantum circuits, *Phys. Rev. Lett.* **119**, 180509 (2017).
- [98] S. Endo, S. C. Benjamin, and Y. Li, Practical quantum error mitigation for near-future applications, *Phys. Rev. X* **8**, 031027 (2018).
- [99] T. Giurgica-Tiron, Y. Hindy, R. LaRose, A. Mari, and W. J. Zeng, Digital zero noise extrapolation for quantum error mitigation, in *2020 IEEE International Conference on Quantum Computing and Engineering (QCE)* (2020) pp. 306–316.
- [100] A. Kandala, K. Temme, A. D. Córcoles, A. Mezzacapo, J. M. Chow, and J. M. Gambetta, Error mitigation extends the computational reach of a noisy quantum processor, *Nature* **567**, 491 (2019).
- [101] S. McArdle, X. Yuan, and S. Benjamin, Error-mitigated digital quantum simulation, *Phys. Rev. Lett.* **122**, 180501 (2019).
- [102] J. Sun, X. Yuan, T. Tsunoda, V. Vedral, S. C. Benjamin, and S. Endo, Mitigating realistic noise in practical noisy intermediate-scale quantum devices, *Phys. Rev. Appl.* **15**, 034026 (2021).
- [103] Y. Kim, C. J. Wood, T. J. Yoder, S. T. Merkel, J. M. Gambetta, K. Temme, and A. Kandala, Scalable error mitigation for noisy quantum circuits produces competitive expectation values, *Nature Physics* , 1 (2023).
- [104] S. Bravyi, S. Sheldon, A. Kandala, D. C. McKay, and J. M. Gambetta, Mitigating measurement errors in multiqubit experiments, *Phys. Rev. A* **103**, 042605 (2021).
- [105] J. R. Wootton, F. Harkins, N. T. Bronn, A. C. Vazquez, A. Phan, and A. T. Asfaw, Teaching quantum computing with an interactive textbook, in *2021 IEEE International Conference on Quantum Computing and Engineering (QCE)* (2021) pp. 385–391.
- [106] P. D. Nation, H. Kang, N. Sundaresan, and J. M. Gambetta, Scalable mitigation of measurement errors on quantum computers, *PRX Quantum* **2**, 040326 (2021).

Appendix S1: Robustness of $\pi/2$ quasienergy spacing in the presence of disorder

In the main text, we discussed that the positive effect of disorder observed near the DTC-thermal phase boundaries is attributed to the preservation of the $\pi/2$ quasienergy spacing among the quadruplets of quasienergies. In this section, we verify this argument by explicitly computing the full quasienergy spectrum of our system (via exact diagonalization) at the same system parameters as those of Fig. 3(c) in the main text. In particular, a quasienergy ε is obtained from the eigenvalue $e^{-i\varepsilon}$ of the (unitary) one-period time evolution operator.

Our results are summarized in Fig. S1, where we have shown some representative quasienergy levels of the system with and without disorders. In particular, for each data point, the blue circle marks the j th quasienergy solution, i.e., ε_j , whereas the corresponding green square (red triangle) marks some other quasienergy solution, e.g., ε_ℓ whose value is the closest to $\varepsilon_j + \pi/2$ ($\varepsilon_j - \pi/2$). Therefore, note that for the many-body quasienergy levels to contain a

macroscopic number of $\pi/2$ -quasienergy separated quadruplets, the majority of the red triangles, green squares, and blue circles in Fig. S1 must coincide with one another. As is clear from the figure, this is the case when disorder is present (panel b). In the absence of disorder (panel a), a significant number of quasienergy solutions do not coincide with any other quasienergy solution when shifted by $\pm\pi/2$. This in turn explains the stronger DTC signal observed in Fig. 3(c) of the main text when disorder is present.

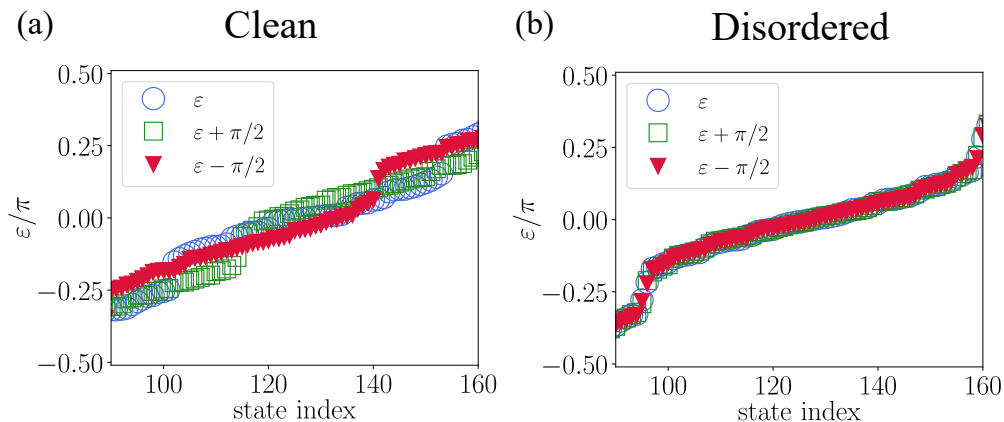


FIG. S1. Representative quasienergy solutions ε (blue circles) and the quasienergies that are closest to them upon shifting by $\pm\pi/2$ (see the discussion of Sec. S1 for the exact definitions) in (a) the absence of disorder and (b) the presence of spatial disorder with $dh = 0.08h, dM = 0.08M$. The system size is taken at $N = 8$ in both panels and all other parameters used are the same as in Fig. 3(c) of the main text, i.e., $JT = 0.13\pi, hT = 0.8\pi, MT = 0.98\pi$. Notably, the degeneracy modulo $\pi/2$ is stronger when disorder is present, thereby explaining the more robust $4T$ -periodicity when disorder is present.

Appendix S2: $4T$ -DTC results for a larger system size of $N = 32$

In this section, we supplement our tMPMs results presented in Figs. 2 and 3 of the main text with those calculated at a larger system size of $N = 32$. Our results, which are summarized in Figs. S2 and S4 of the Supplementary Materials, display qualitatively the same features as those obtained in the main text. That is, the period-quadrupling signature of the $4T$ -DTC is not only robust against a variety of spatial disorders (see Fig. S2), but it may get amplified in some cases (see Fig. S4).

Appendix S3: Finite-size effect analysis

For completeness, Fig. S3 demonstrates the finite-size effect analysis for the signatures of $4T$ -DTC. Indeed, supporting the observation we made in the main text, both deep in the DTC regime and near the border with the thermal phase, the magnetization profile appears to be qualitatively the same for all system sizes. Upon closer inspection, one might observe a slight decrease in the magnetization amplitude with the system size which is vaguely visible near the border with the thermal phase and is virtually invisible deep in the DTC regime. This observation could be understood from the many-body quasienergy structure in the spirit of Fig. 3b. In particular, recall that the many-body quasienergy of a $4T$ -DTC system forms quartets with $\omega/4$ separation ($\pi/2$ when taking $T = 1$). Perturbations in the system parameters tend to hybridize some pairs of quasienergy eigenstates belonging to different quartets, thereby slightly shifting them in quasienergies which then leads to imperfect $\omega/4$ separation. This explains the decrease in the magnetization amplitude as one moves towards the DTC-thermal phase boundaries. As larger system sizes correspond to larger numbers of many-body quasienergy eigenstates, more hybridization events occur and consequently leads to more imperfect $\omega/4$ separation. That said, such a hybridization mechanism is generally very weak for quasienergy eigenstates that are well separated in quasienergy. These in turn explain the observed small decrease in the magnetization amplitude with the system size at fixed system parameter values. Nevertheless, as this decrease is very small and almost unnoticeable in the figure, the case $N = 8$ we considered in the main text has already captured the most dominant hybridization event.

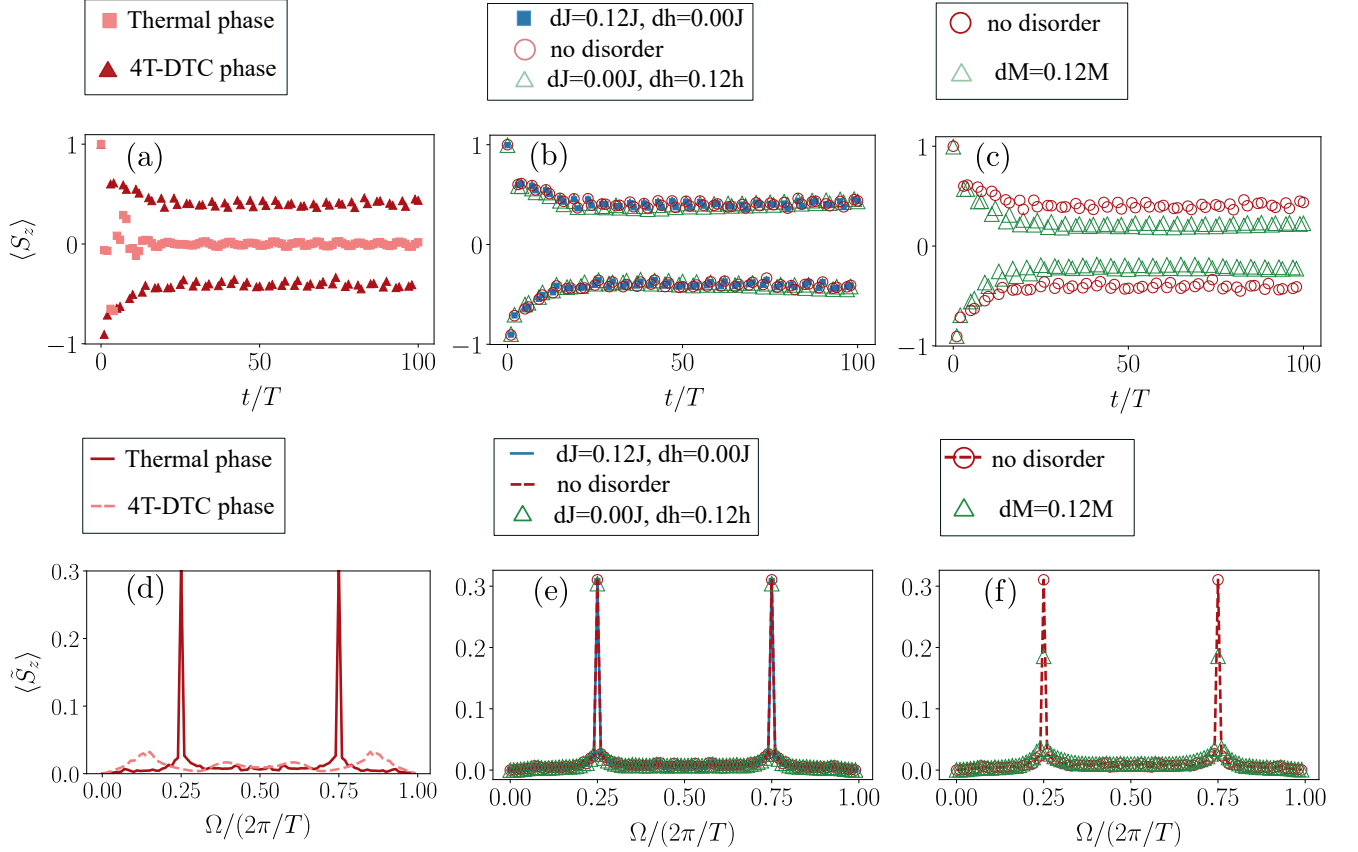


FIG. S2. Numerical evidence of robust $4T$ -DTC for $N = 32$ sites using tMPS. (a)-(c) Stroboscopic magnetization $\langle S_z \rangle$ as a function of time. (d)-(f) The power spectrum $\langle \tilde{S}_z \rangle$. In panel a and d, the darker red data is taken at $J = 0.16\pi$, $M = 0.98\pi$, and $h = 0.9\pi$ (which corresponds to the $4T$ -DTC phase regime in Fig. 3(a) of the main text), and the lighter red data is taken at $J = 0.1\pi$, $M = 0.98\pi$, and $h = 0.52\pi$ (which corresponds to the thermal phase regime in Fig. 3(a) of the main text). In panel b and e, the data points correspond to no disorder (red), $dh = 0.12h$ (green), and $dJ = 0.12J$ (blue). In panel c and f, the data points are taken at no disorder (red) and $dM = 0.12M$ (green). In all panels, the system size is $N = 32$, T is set to be 1, and all disorder results are averaged over 220 disorder realizations, each of which is equally drawn from the corresponding interval. Numerically, it is found that for larger system size such as $N = 32$, our $4T$ -DTC model is still robust against a variety of spatial disorders.

Appendix S4: Variational algorithm for the time evolution on IBM Q

In this section, we describe our implementation of the variational algorithm to perform the time evolution of our model in the main text on digital quantum computers, specifically the IBM Q quantum processors.

1. Details of the IBM quantum processor and its error rates

First, we show the details of error and the choices of qubits on the 27-qubit Falcon IBM quantum processor *ibmq-cairo*, which we have utilized throughout this work. The error profile of the device is shown Fig. S5(a), encompassing both CX (CNOT) gate errors as well as readout assignment errors, as depicted by the colors in the circles (readout assignment errors) and the bonds (gate errors). In Fig. S5(b), we show the choice of $N = 8 + 1$ qubits (grey circles) which we used to represent our system, indexed 0 to 8, which is consistent with the circuit configuration in the main text.

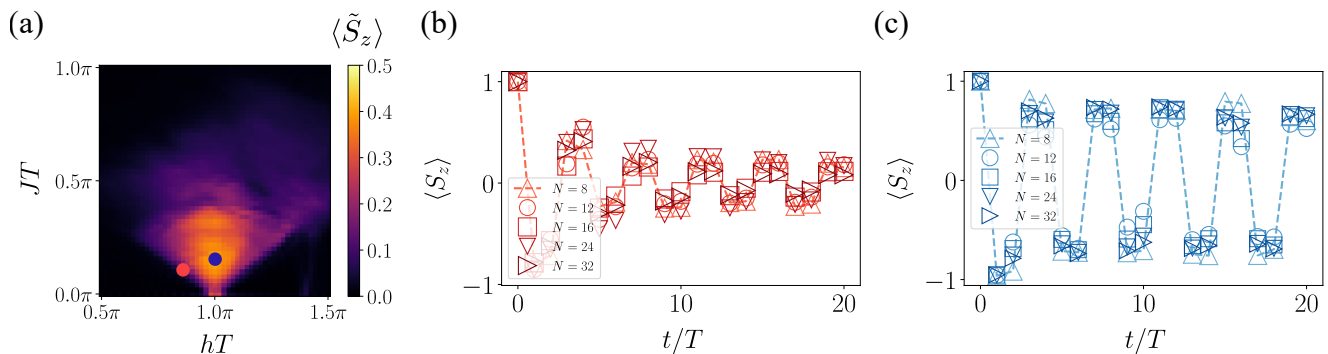


FIG. S3. Finite-size effect analysis: (a) The phase diagram representing the value of the subharmonic peak at $\Omega T = \pi/2$ and $MT = 0.98\pi$ for $N = 16$ as an example. We also plotted the magnetization $\langle S_z \rangle$ as a function of time for (b) DTC-thermal phase boundary at $JT = 0.14\pi, MT = 0.98\pi, hT = 0.8\pi$ [red dot in panel (a)], and for (c) 4T-DTC phase at $JT = 0.16\pi, MT = 0.98\pi, hT = \pi$ [blue dot in panel (a)] both for different system size $N = 8, 12, 16, 24$ and 32 using tMPS.

2. Additional details of the variational circuit recompilation of the time evolution operators

In the current NISQ-era of quantum computing, variational quantum algorithms (VQAs) have proven to be effective due to their reduced gate counts, as discussed in references [81, 82]. VQAs involve a two-step process where parameterized circuits are first generated on a classical computer through an optimization algorithm. Then, these circuits with optimized parameters are executed on the quantum computer. Therefore, we explore a variational approach referred to as 'circuit recompilation' (detailed in references [83–87]), which has shown promise in providing accurate approximations to the original unitary transformations while requiring much shorter circuit depths and fewer CX and single-qubit gates compared to the default isometry decomposition. This approach results in significantly reduced overall gate errors when using current NISQ-era quantum processors [49].

As described in the main text, the variational circuit in this work consists of an initial layer of U_3 gates followed by concatenated odd layers (green) and even layers (purple) [83, 84, 86, 88, 89] [Fig. S5(c)], which has a Trotterized time evolution pattern. We also follow the definitions of 3D rotation U_3 gates from Qiskit [90]:

$$U_3(\theta, \phi, \lambda) = \begin{pmatrix} \cos\left(\frac{\theta}{2}\right) & -e^{i\lambda} \sin\left(\frac{\theta}{2}\right) \\ e^{i\phi} \sin\left(\frac{\theta}{2}\right) & e^{i(\phi+\lambda)} \cos\left(\frac{\theta}{2}\right) \end{pmatrix} \quad (\text{S1})$$

where $\theta, \phi, \lambda \in [0, 2\pi]$.

The optimization of the quantum circuits is carried out using the Limited Memory Broyden-Fletcher-Goldfarb-Shanno algorithm with box constraints (L-BFGSB), as outlined in Refs. [86, 91, 92]. To prevent getting stuck in local minimums during the optimization, we employ a basin-hopping technique [93–96]. Here, small perturbations are introduced in each optimization iteration, which are then followed by local minimization steps.

In addition, due to the IBM quantum device configuration geometry, an additional ancilla qubit [green circle, Fig. S5(d)] is required such that the Heisenberg spin zz interactions can be realized with one CX gate plus two swap gates on IBM Q [Fig. S5(d)], and therefore the model configuration with $N = 8$ (system) +1 (ancilla qubit) is consistent with the device [Fig. S5(b)]. To simulate a larger system size, encompassing more than 10 qubits, our model described by Eq. (1) in the main text is inherently scalable. It can be mapped to a two coupled one-dimensional chains, where each unit cell consists of two sites labeled as a and b . In this case, the interactions between a sites become next-nearest-neighbor-couplings. Such a setup can be easily achieved via the technique of circuit recompilation [86].

3. Error mitigation on IBM Q

One major issue we address in our IBM Q experiment is the readout assignment error [see also Fig. S5(a)]. This issue involves the possibility of mistakenly measuring an $|\uparrow\rangle$ state as $|\downarrow\rangle$ and vice versa. Recent advancements have made significant progress in reducing measurement errors, as documented in several studies [97–103]. In the context of the Qiskit environment [90], one approach involves running calibration circuits with various initial conditions and then using the resulting data to estimate accurate measurement counts based on a calibration matrix [104, 105]. However, in our paper, we employ a novel readout error mitigation method [106] that requires only a small number

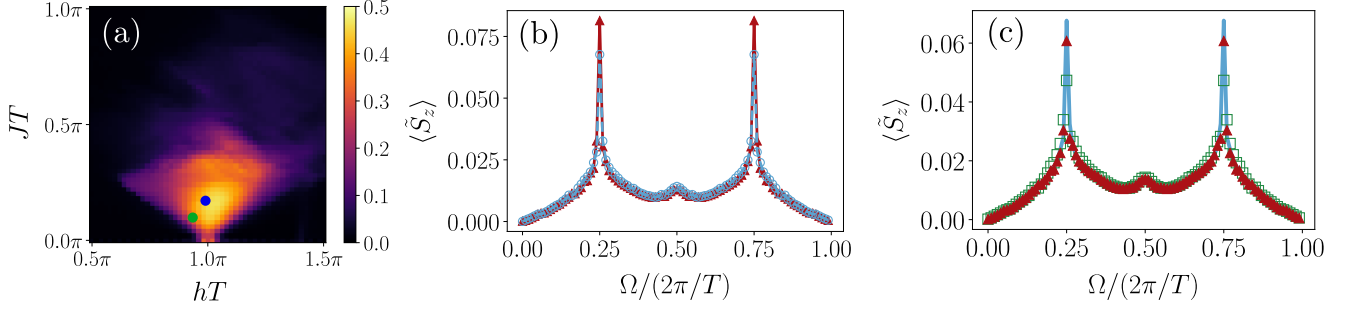


FIG. S4. (a) The phase diagram representing the value of the subharmonic peak at $\Omega = \pi/2$ and $MT = 0.98\pi$, numerically computed for a large $N = 32$ system size. The $4T$ -DTC phase is nearly symmetric, and spans over a considerable window of h values, which are symmetric about $hT = \pi$ and at moderate values of J . The green dot corresponds to the parameter values used in (b,c), whereas the blue dot corresponds to the parameter values used in Fig. S2(b), (c), (e) and (f). (b,c) The numerically calculated power spectrum $\langle \tilde{S}_z \rangle$ over 100 periods at $JT = 0.13\pi$, $hT = 0.8\pi$, $MT = 0.98\pi$ with (b) no disorder (blue); $dh = 0.08h$ (red). (c) without disorder (blue); only $dM = 0.04M$ (green); both $dM = 0.04M$ and $dh = 0.08h$ (red). The system size is taken at $N = 32$ in all panels and all data points involving disorders in panels b and c are averaged over 220 disorder realizations. From the power spectrum peak in panel (b) at $\Omega T = \pi/2$, it is shown that the period-quadrupling signature of the $4T$ -DTC is also enhanced by the spatial disorder dh .

of circuits, eliminating the need to construct a full calibration matrix, and is ready to use with their Python package integrated with the Qiskit environment [90].

To align with the job submission framework of the IBM Q platform and optimize the calibration process, we combine the circuits responsible for performing the time evolution (referred to as "physical circuits") with the calibration circuits as mentioned above into a single job submitted to the IBM Q cloud platform. This ensures that the physical circuits and calibration circuits are executed nearly simultaneously, enhancing the accuracy of the calibration process. Additionally, to maintain a consistent quantum register layout for both physical and calibration circuits, we first select and transpile the physical circuit for the specific real device using device error data calibrated by IBM Q for high-fidelity quantum nondemolition (QND) measurements [86]. We then apply this layout to the calibration circuit, ensuring that the same qubits are used for both categories of circuits. Finally, we submit both types of circuits together to the IBM Q real device for execution.

4. Additional results for noisy simulations

In this section, we present additional simulation results that highlight the impact of noise on the IBM Q processor, and subsequently the critical role of our variational approach that was primarily employed in the main text. To this end, our results in this section were also obtained using the more conventional Trotterization approach, similar to what we demonstrated with our tMPS results. The comparison of these results with that obtained using the variational approach is presented in Fig. S5. In the quantum processor used for our simulations, the average error rate for CX gates is approximately 10^2 , which significantly impacts the noisy simulations based on Trotterization approach. This is particularly evident in the comparison between the yellow and blue curves in Fig. S6, where the noise present in the quantum processor is too large for the Trotterization approach to yield the expected $4T$ -oscillation. This clearly shows the significant advantage of our variational approach over the Trotterization approach for simulating our $4T$ -DTC system with 8 qubits.

It is worth noting that at larger system sizes, there is no guarantee anymore that our variational approach is still advantageous over the Trotterization approach, since two major challenges are at play. On the one hand, the exponential increase in complexity means that achieving good convergence in our variational approach becomes computationally expensive. On the other hand, the noise effects become even more pronounced when more qubits are involved. In particular, if noise could be reduced in future quantum processors, the Trotterization approach may become preferable over the variational approach. In Fig. S6, we also show some results obtained from a local noise simulator under the Trotterization approach with a controllable error rate, from which we observe that a single-qubit error rate of around 10^{-3} or below is required to yield a clear $4T$ -oscillation. Given that the latest IBM Q processor achieves a single-qubit error rate of 5×10^{-3} , it is expected that a realization of our system at larger system sizes and without the use of variational approach becomes possible in the near future. However, it should be stressed that with the current technology, our variational approach is potentially the most feasible method to verify our $4T$ -DTC

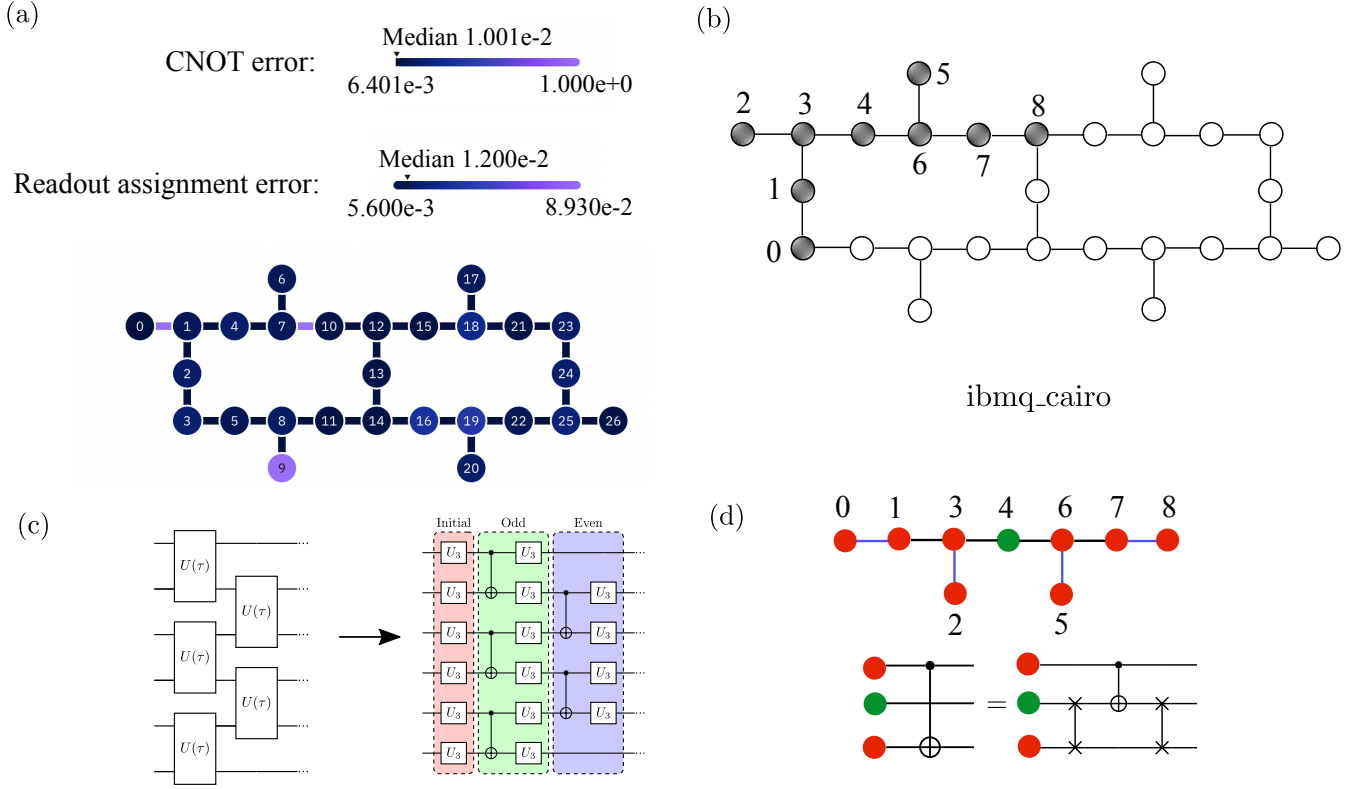


FIG. S5. The geometry and error information of IBM Q device *ibmq_cairo* and details of the variational circuit recompilation algorithm. (a) The snapshot taken from IBM Q (on June 20, 2023) for CNOT (CX) gate error and readout error. Here, the readout error is represented by the coloring on the qubit sites, whereas the CX gate error is represented by the coloring on the links connecting nearest-neighboring qubits. (b) An example of qubits choices (grey circles) of which the geometry is consistent with the configuration shown in panel (d). (c) The quantum circuit for the Trotterized time evolution is transformed into a parameterized quantum circuit suitable for execution on an IBM quantum processor via optimization on a classical computer. See also details in Ref. [83, 84, 86, 88, 89] (d) (upper panel) The configuration of the quantum circuit with the additional ancilla qubit. (lower panel) The next-to-nearest neighbor CX gate can be exactly decomposed to nearest-neighbor two-body gates.

signatures at the relatively small number of qubits. Most importantly, such an approach could also be potentially utilized to simulate other quantum many-body systems whose properties are observable at a similar number of qubits.

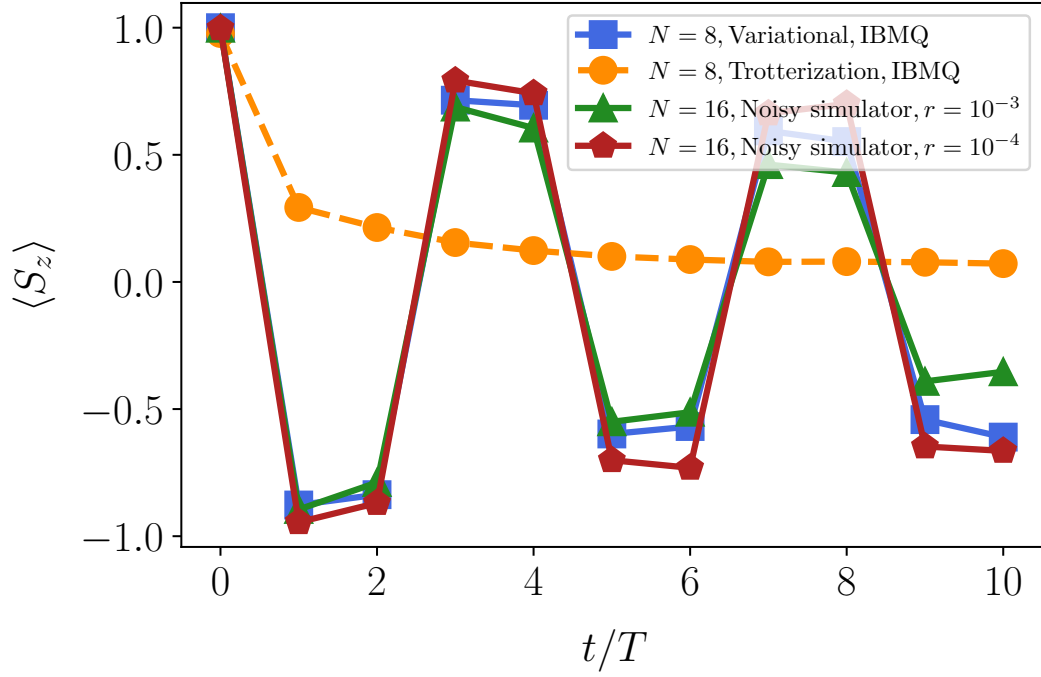


FIG. S6. Characterization of noisy effects. We present the noisy simulation on two kinds of simulators: blue and yellow curves for simulations on the real IBM Q processor; green (Trotterization approach with single-qubit gate error rate $r = 10^{-3}$ shown in Fig. S5 (c)) and red (Trotterization approach with single-qubit gate error rate $r = 10^{-4}$) curves for simulations on the classical Aer simulator [90] with a controllable error rate r .